



Full Length Article

The influence of Y additions on the microstructure and mechanical properties of MoTaWNb refractory high entropy alloy films by magnetron sputtering

Cong Fang ^{a,b}, Chao Zhang ^{a,b,*}, Shuaishuai Zhu ^{a,b}, Baosen Zhang ^{a,b,*}, Yuxing Fan ^{a,b}^a School of Materials Science and Engineering, Nanjing Institute of Technology, Nanjing 211167, China^b Jiangsu Key Laboratory of Advanced Structural Materials and Application Technology, Nanjing 211167, China

ARTICLE INFO

ABSTRACT

Keywords:

High entropy amorphous alloy
Film
Microstructure
Frictional behaviors

The films of $(\text{MoTaWNb})_{1-x}Y_x$ high entropy amorphous alloy were successfully deposited by direct current magnetron sputtering under different contents of Y additions. The microstructure, mechanical properties, and friction behaviors of the as-deposited $(\text{MoTaWNb})_{1-x}Y_x$ films were investigated. The results show that the films were mainly composed of amorphous and body-centered cubic (BCC) phases, and the proportion of the amorphous phase increases gradually with the increase in Y content. When the deposited film has a typical amorphous phase with a uniform and dense fibrous-shaped columnar microstructure, it shows a maximum nano-hardness of 6.74 GPa. However, the growth of V-shaped columnar microstructures during film deposition increases its surface roughness and decreases its mechanical properties. Abrasion wear, oxidation wear, and delamination wear dominate the wear process, and the evolution of the frictional behaviors of deposited films is directly related to their structural and mechanical changes. The wear resistance of $(\text{MoTaWNb})_{1-x}Y_x$ films with wear rates of the order of $10^{-5} \text{ mm}^3 \cdot \text{N}^{-1} \cdot \text{m}^{-1}$ is achieved by tuning the Y additions, and this film can be used as a potential candidate for wear-resistant coatings.

1. Introduction

A new type of alloy material known as high entropy amorphous alloy is distinguished by its multi-component composition of high-entropy alloys (HEAs) and its amorphous structure [1]. High entropy amorphous alloys have good strength and hardness, as well as good resistance to corrosion and wear, because of their homogeneous chemical composition, simple microstructure, macroscopic isotropy, and lack of element segregation. According to a related study, the possibility that an alloy would develop an amorphous structure increases with the number of alloy group elements and the degree of disorder [2]. Research on high entropy amorphous alloys has since been conducted and is still developing. For example, the $\text{Zn}_{20}\text{Ca}_{20}\text{Sr}_{20}\text{Yb}_{20}(\text{Li}_{0.55}\text{Mg}_{0.45})_{20}$ amorphous alloy exhibits significant uniform deformation without shear bands under room temperature stresses [3]. The glass-forming ability (GFA) of $(\text{Co}_{0.33}\text{Ni}_{0.33}\text{Cr}_{0.23}\text{Mo}_{0.1})_{80-x}\text{Nb}_x(\text{B}_{0.3}\text{Si}_{0.7})_{20}$ high entropy amorphous coatings can be significantly improved by increasing the Nb content, and the Vickers hardness can reach up to 707.9 HV [4]. The bulk amorphous $\text{Fe}_{25}\text{Co}_{25}\text{Ni}_{25}(\text{P}, \text{C}, \text{B}, \text{Si})_{25}$ alloy has outstanding GFA, a maximum

critical diameter of up to 2 mm, and superior soft magnetic and mechanical characteristics [5]. The $\text{Co}_{34}\text{Cr}_{29}\text{B}_{14}\text{Fe}_8\text{Ni}_8\text{Si}_7$ amorphous coating was created using laser cladding technology, and the results showed that the coating's micro-hardness, wear resistance, and corrosion resistance increased with its amorphous content [6].

Currently, the most common forms of high entropy amorphous alloys are powders, wires, foil strips, and other small sizes because of the difficult preparation process and the limitations of GFA. As a result, the preparation of high entropy amorphous films on the substrate as protective and functional films becomes the best choice. One of the most popular techniques for creating high entropy amorphous films is magnetron sputtering (MS), which allows for flexible control over the process parameters and target composition to produce films with a high deposition rate and excellent bond strength. Furthermore, MS has a rapid cooling rate ($\sim 10^9 \text{ K/s}$) that promotes the production of amorphous phases [7,8]. Using reactive magnetron sputtering, Cui et al. [9] synthesized $(\text{AlCrTiZrHf})\text{N}$ high entropy amorphous alloy nitride films. The formation of the amorphous state was primarily caused by high mixing entropy and a large atomic size difference. Additionally, solid

* Corresponding authors at: School of Materials Science and Engineering, Nanjing Institute of Technology, Nanjing 211167, China.

E-mail addresses: zhangchao@njit.edu.cn (C. Zhang), baosenzhang@njit.edu.cn (B. Zhang).

solution strengthening of various elements and the formation of a saturated metal nitride phase resulted in the hardness and modulus of elasticity of the thin films at 33.1 GPa and 347.3 GPa when the N₂:Ar ratio was 5:4. Amorphous films like CrNbTiMoZr [10], AlSiTaTiZr [11], and BNbTaTiZr [12], which show exceptional wear resistance and thermal stability, can also have their mechanical and high-temperature properties effectively improved by adding high melting point elements like Nb, Ta, Mo, W, Ti, Zr, and Hf to the main elements. The WNbMoTa and WNbMoTaV as-cast equiautomatic-ratio refractory HEAs feature a single-phase BCC structure, ultra-high hardness of Hv = 4455 MPa and Hv = 5250 MPa, respectively, and exceptional compression-plastic strain properties at temperatures above 600 °C [13,14].

Because of its exceptional physical and chemical characteristics, rare earth yttrium is frequently employed as an additive in the field of alloy modification. These attributes allow the yttrium element to efficiently modify the structure of an alloy and maximize its performance. According to related research, rare earth elements actively contribute to the toughening of HEAs by purifying or generating a second phase at grain boundaries. With the addition of Y, the network-structured borides in the FeCoNiAlCrB alloy are greatly refined and dispersed at the boundary of the BCC phase, which leads to an increase in the alloy fracture toughness of about 50 % but only a decrease in the Vickers hardness of about 10 % [15]. According to reports, the GFA of alloys is significantly impacted by the inclusion of rare earth metals, and the addition of Y can successfully prevent the formation of the crystalline phase. Cu₄₆Zr₄₂Al₇Y₅ amorphous alloys with diameters larger than 1 cm can be easily obtained by injection mold casting, and the excellent GFA mainly comes from the alloying effect of Y, which can effectively reduce the liquid phase line temperature of the alloys and make the compositions closer to quaternary eutectics [16]. Hong et al. [17] discovered that while Y increased the GFA of the CuZrAl alloy system, Y also caused a decrease in binding energy, which resulted in a decrease in fracture strength. Lu et al. [18] investigated the effect of alloyed Y on the high-temperature oxidation behavior of AlMo_{0.5}NbTa_{0.5}TiZr alloys, and the addition of 0.6 at.% Y was able to significantly improve the oxidation resistance of the alloy. However, the high content of Y (1 at.%) causes high localized stresses and cracks induced by the rapid aggregate oxidation of the Al₃Y₅ phase and reduces the high-temperature oxidation resistance of the alloy. The atomic size difference and lattice distortion of the FeCoNi_{1.5}CuB HEAs increase with the addition of the Y element, improving the alloy's compressive and yield strengths. This improvement is primarily attributable to the alloy's solid solution, fine grain, and dispersion strengthening following the addition of Y [19]. Wang et al. [20] found that the substrate bias has a significant effect on the microstructure and properties of the deposited films. The ZrNbTiMo refractory high entropy alloy (RHEA) films consist of both nanocrystalline and amorphous phases and exhibit a maximum value of 21.3 GPa of hardness at -200 V, while a unique mechanism of inter-column sliding deformation allows the film to exhibit excellent wear resistance. Different crystal-amorphous transition characteristics of RHEA films can be caused by the addition of Y. However, the influence of Y addition on the mechanical properties and nanocrystalline-amorphous phase transition behavior of MoTaWNb RHEA films has rarely been investigated.

In this study, (MoTaWNb)_{1-x}Y_x RHEA films were prepared using MS from dual targets of MoTaWNb and Y, and the contents of Y in RHEA films were adjusted by sputtering powers of the Y target. The influences of composition and microstructure with varying Y contents in these RHEA films were characterized. The mechanical properties and tribological characteristics of the films were analyzed to demonstrate the feasibility of using them as coating materials with high strength and reliability.

Table 1
The parameters of magnetron sputtering deposition.

Parameters	Values
Atmosphere	Ar
Background vacuum (Pa)	8 × 10 ⁻⁴
Argon gas flow (sccm)	30
Substrate rotation speed (rpm)	10
Deposition pressure (Pa)	2.0
Distances of target to substrate (mm)	100
Bias of substrate (V)	0
Deposition duration (min)	90

2. Experiments

2.1. Film preparation

On silicon wafer substrates, the films of (MoTaWNb)_{1-x}Y_x RHEA were deposited using DC dual-target MS (MSP-300B, China). Both the Y target and the isoatomic ratio of Mo₂₅Ta₂₅W₂₅Nb₂₅ (in at.%) (RHEA) target have a high level of purity ($\geq 99.9\%$), and the targets have a diameter of 60 mm and a thickness of 5 mm. The substrate of the N-typed Si (100, 15 mm × 15 mm) wafer was ultrasonically cleaned in acetone and anhydrous ethanol for 20 min, respectively, to get rid of surface oils and contaminants before deposition. Next, the targets were pre-sputtered for 10 min to remove surface oxides. The deposition parameters are shown in Table 1. The bias voltage and heating of substrate were absent during film deposition. The sputtering power of the MoTaWNb target was maintained at 100 W, which was noteworthy. By altering the sputtering power (0, 20, 40, 60, and 80 W) of the Y target, the elemental content of the films was changed.

2.2. Film characterization

The phases of the films were analyzed by Cu-K_α X-ray diffraction (XRD, Rigaku Ultima IV) at 40 kV and 40 mA. The test range was 20° ~ 65°, the scanning speed was 4°/min, and the step size was 0.02°. The thickness, chemical composition, and microstructure of the films were characterized using field emission scanning electron microscopy (FE-SEM) fitted with an energy dispersive spectrometer detector (EDS). The specimen preparation for TEM analysis was prepared using focused ion beam SEM (FIB-SEM, Helios NanoLab 650, FEI, USA). The structure of the films was evaluated by high-resolution transmission electron microscopy (HRTEM, Talos F200X) with an accelerating voltage of 200 kV. During TEM observation, the dispersion of alloying elements and compositional data were observed using energy-dispersive X-ray spectroscopy (EDX) with compositional mapping. The surface morphology and surface roughness of the films were determined using the non-contact mode of the atomic force microscope (AFM) and a scanning area of 10 × 10 μm. The hardness and Young's modulus of the films were obtained by nanoindentation (Agilent G200) using a Berkovich diamond indenter at room temperature, and the displacement of the indenter was limited to 500 nm. The continuous stiffness measurement (CSM) was utilized to accurately derive the film properties. This method can be used to continuously measure a material's hardness and modulus of elasticity as a function of depth without the need for discrete unloading cycles. The average results were calculated by measuring more than ten points per sample. Furthermore, the friction and wear performances were tested at room temperature using a multifunctional tribometer (Rtec) and grinding balls of approximately 12.7 mm in diameter made of Si₃N₄. The constant applied normal load was 0.2 N, and the sliding speed was 20 mm/s with durations of 600 s. A 3D profiler (Rtec, Micro-XAM) was used to measure wear volume. Using the following formula, the wear rate (W_r) was determined: W_r = V/FS, where V stands for volume loss, F for load, and S for total sliding distance.

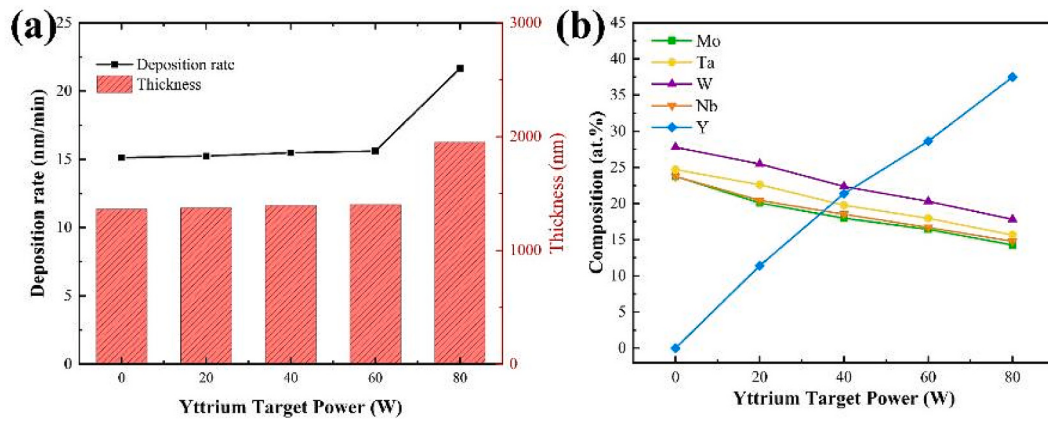


Fig. 1. Deposition rate and chemical composition of $(\text{MoTaWNb})_{1-x}\text{Y}_x$ films at different Y-target power.

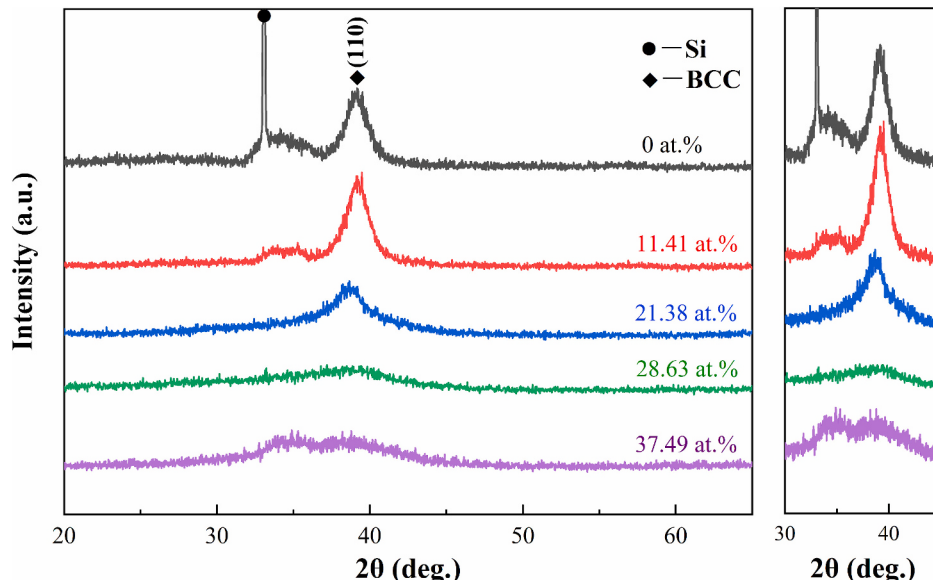


Fig. 2. XRD patterns of $(\text{MoTaWNb})_{1-x}\text{Y}_x$ RHEA films with different Y content.

3. Results and discussion

3.1. Deposition rate and chemical composition of films

The deposition rate and chemical composition of as-deposited $(\text{MoTaWNb})_{1-x}\text{Y}_x$ films are shown in Fig. 1. With the Y-target power enhancement, the thickness of the deposited film increases gradually as well. The deposition rate of the film is closely correlated with power, maintaining a stable linear growth trend from 0 to 60 W before abruptly increasing to 21.67 nm/min at 80 W. This is primarily because an increase in sputtering power results in a marked improvement in the rate of argon ionization and an increase in ion energy. This increases the deposition rate at which target atoms are bombarded and the number of deposited atoms that reach the substrate in a given amount of time [21]. The sputtering yield of the Y element is discovered to be much bigger than that of the Ta and W elements under Ar ion bombardment at energies < 1000 eV, and a surge interval appears for the sputtering yield of the Y target with rising power [22]. Trace levels of elemental O were discovered in the films, which can be attributed to the fact that oxygen is hard to remove by sputter-cleaning, and the oxygen probably stems from the oxides on the substrate surface, the residual gases, and impurities in the target [23]. The chemical compositions (at.%) of the films, measured by EDS, were approximately equal to the nominal equiatomic

percentage of 25 at.% for Mo, Ta, W, and Nb elements of the target, as shown in Fig. 1b. It is noteworthy that the atomic content of Ta and W is higher than that of the thin-film elements Mo and Nb. The primary causes of this are that light atoms hit by Ar + are unstable in flight before deposition and more prone to scattering, and the relative atomic masses of Mo and Nb are smaller than those of Ta and W. Second, the atoms are constantly colliding as they accumulate during the deposition process. When their kinetic energy exceeds the surface binding energy, the atoms can separate from the substrate, and comparatively light atoms like Mo, Nb, etc. are more likely to accumulate enough momentum to be scattered [10,24]. By increasing the power of Y, the element content of Y in films increases linearly. When the power ranges from 0 to 80 W, Y content increases quickly to reach 21 at.%, then slowly rises to 37 at.% at 80 W. The content of other elements is about 15–23 at.%.

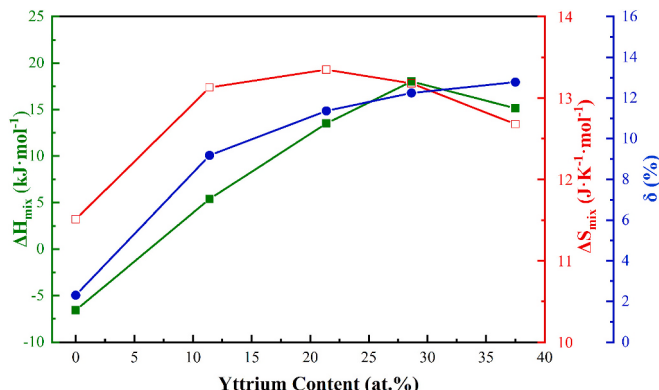
3.2. Phase and structure of films

Fig. 2 shows the XRD patterns of the deposited films with different Y contents. Due to the film's thickness and the ease with which X-rays can pass through the sample to the substrate, a distinct diffraction peak from the Si substrate can be seen at approximately 33°. It is observed that the as-deposited MoTaNb has a broad (110) diffraction peak at 39.4°, presenting a single BCC phase. The major phase of these films shows

Table 2

The values of atomic radius and mixing enthalpy of element pairs [[26,27].]

Element	Atomic radius (Å)	ΔH_{mix} (kJ/mol)				
		Mo	Ta	W	Nb	Y
Mo	1.363	0	-5	0	-6	24
Ta	1.430	-	0	-7	0	27
W	1.367	-	-	0	-8	24
Nb	1.429	-	-	-	0	30
Y	1.802	-	-	-	-	0

**Fig. 3.** The calculated thermodynamic parameter values of $(\text{MoTaWNb})_{1-x}\text{Y}_x$ RHEA films.

nanocrystalline and amorphous dual phases when Y content is <21.4 at. %, as indicated by a halo-shaped peak present in the range of $36\text{--}44^\circ$ at 2θ . It implies that crystalline nano-domains may be present, but the X-ray diffraction technique is not relevant to characterizing them. By increasing the Y content, the intensity of the diffraction peak decreases significantly, which reveals that the addition of Y promotes the formation of the amorphous phase of the films. The crystallinity of the deposited films can be roughly quantitatively analyzed by XRD peak fitting. The results show that the relative contents of the crystallization phases of 0, 11.41, 21.38 at.% Y-added RHEA films are 51.78 %, 14.97 % and 4.62 %, respectively. In addition, the crystallinity of films is roughly 0 % when the Y contents are >21.38 at.%, indicating that the phases of these RHEA films are completely amorphous. This can be attributed to the fact that Y has an atomic radius that is significantly bigger than that of Mo, Ta, W, and Nb, resulting in an increment of the degree of lattice distortion. Moreover, the atomic radius and mixing enthalpy (ΔH_{mix})

values of the film elements are shown in **Table 2**. Research on constituent phases in HEAs systems has revealed that three parameters primarily predict the phase selection of amorphous, solid solution, and intermetallic phases: atomic size difference (δ), mixing enthalpy (ΔH_{mix}), and mixing entropy (ΔS_{mix}), which are defined as:

$$\delta = 100 \sqrt{\sum_{i=1}^n c_i (1 - r_i / \bar{r})^2} \quad (1)$$

$$\Delta H_{\text{mix}} = \sum_{i=1, i \neq j}^n \Omega_{ij} c_i c_j \quad (2)$$

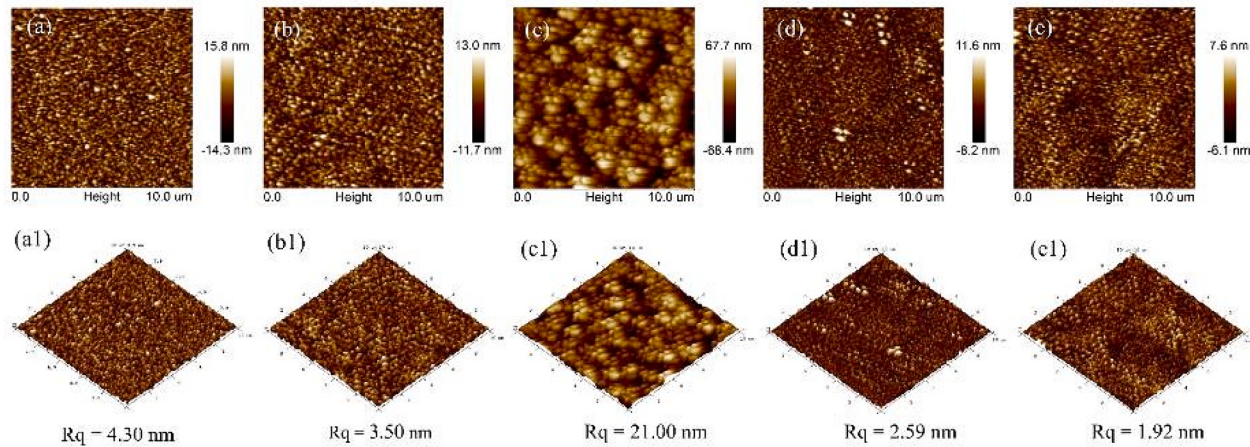
$$\Delta S_{\text{mix}} = -R \sum_{i=1}^n c_i \ln c_i \quad (3)$$

where $\bar{r} = \sum_{i=1}^n c_i r_i$, c_i and r_i are the atomic percentage and atomic radius of the i th element. Where $\Omega_{ij} = 4\Delta_{\text{mix}}^{AB}$, $4\Delta_{\text{mix}}^{AB}$ is the mixing enthalpy of binary liquid AB alloys. Where R is the gas constant [25,26].

The thermodynamic parameter values of $(\text{MoTaWNb})_{1-x}\text{Y}_x$ RHEA films are shown in **Fig. 3**. The findings demonstrate a significant reliance of the film's thermodynamic characteristics on its Y concentration. The deposited films exhibit a growing elemental Y content, with ΔH_{mix} and ΔS_{mix} appearing to increase and thereafter drop, whereas δ displays an increasing trend. Large atomic size differences cause significant strain energy increases and lattice distortions. This allows deposited atoms to diffuse slowly, slowing down grain growth and forming amorphous and nanocrystalline formations. Simultaneously, Gibbs free energy can be greatly reduced by a high ΔS_{mix} and a lower negative ΔH_{mix} . This lessens the inclination to form ordered phases and intermetallic compounds, which promotes the formation of amorphous phases in alloys [26]. Studies on high entropy amorphous thin films are currently rare, but it is clear that preparing amorphous thin-film materials is much simpler than preparing amorphous bulk. This is primarily because vapor deposition techniques are more likely to meet the external conditions of the amorphous phase, such as a high degree of sub-cooling and a low atomic diffusion rate, and a sufficiently fast cooling rate permits the suppression of crystal nuclei's formation and growth while retaining the majority of high-temperature melt alloys' disordered structures [28].

3.3. Morphology analysis of films

Top-surface two-dimensional and three-dimensional AFM images of the $(\text{MoTaWNb})_{1-x}\text{Y}_x$ RHEA films are presented in **Fig. 4**. The MoTaWNb film without Y presents a granular particle morphology surface with an

**Fig. 4.** 2D and 3D images of AFM showing the surface roughness of $(\text{MoTaWNb})_{1-x}\text{Y}_x$ RHEA films with different Y content: (a) (a1) 0 at.% Y, (b) (b1) 11.41 at.% Y, (c) (c1) 21.38 at.% Y, (d) (d1) 28.63 at.% Y, and (e) (e1) 37.49 at.% Y.

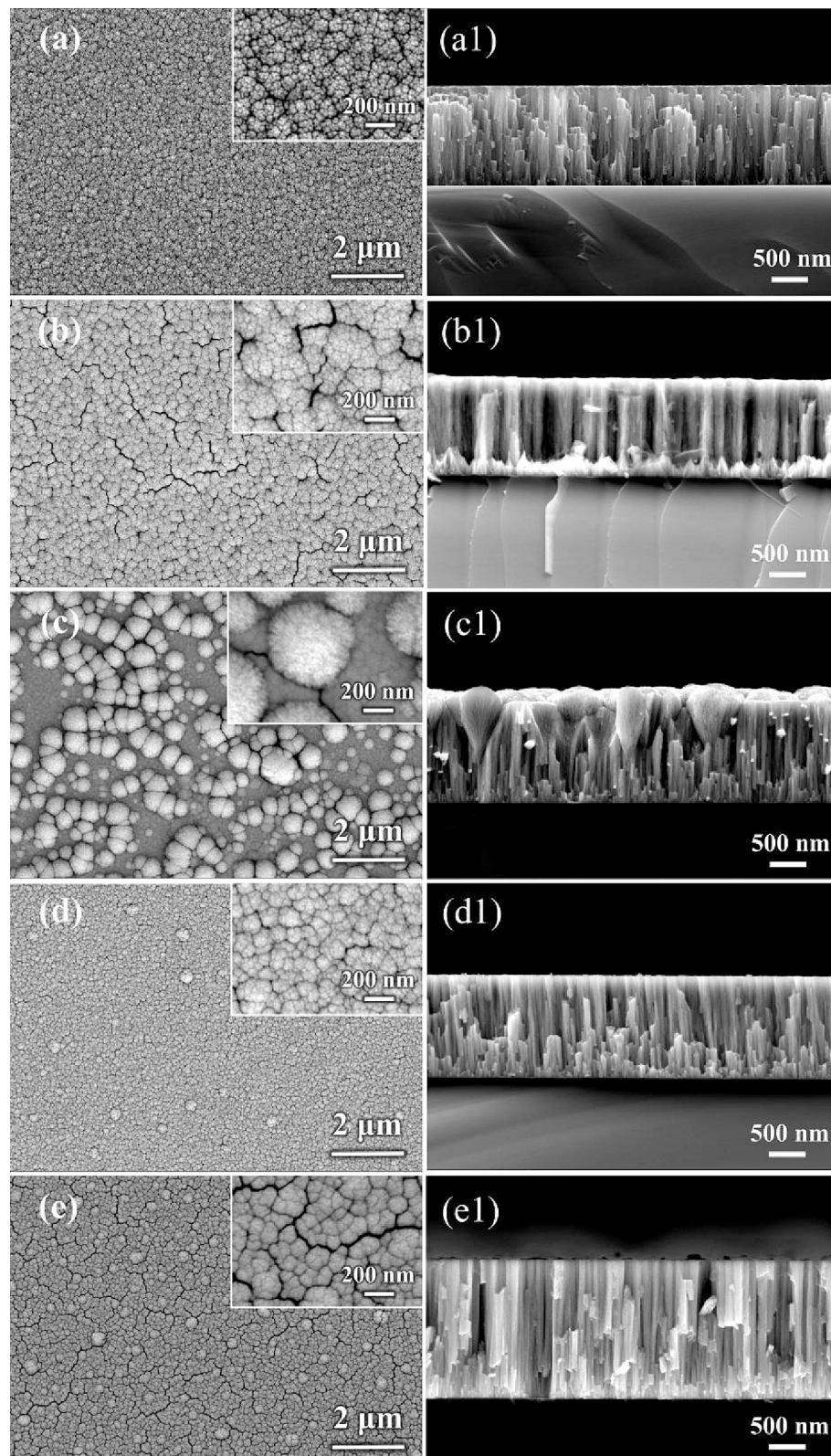


Fig. 5. Cross-section and surface SEM images of $(\text{MoTaWNb})_{1-x}\text{Y}_x$ RHEA films with different Y content: (a) (a1) 0 at.% Y, (b) (b1) 11.41 at.% Y, (c) (c1) 21.38 at.% Y, (d) (d1) 28.63 at.% Y, and (e) (e1) 37.49 at.% Y.

average root mean square (RMS) of about 4.3 nm. As the Y contents increase to 21.38 at.%, the roughness of the film decreases to 3.5 nm and then increases to 21.0 nm significantly. This may be attributed to the change to the V-shaped columnar growth mode, which is investigated by SEM and TEM analysis subsequently. With the Y content increasing from

28.63 at.% to 37.49 at.%, the RHEA film's surface becomes smoother, and the roughness of the films decreases from 2.59 to 1.92 nm, probably owing to the refining of the particle size and amorphization. It can be reasonable that thin film with an amorphous structure possesses lower RMS roughness as compared to its crystalline counterpart.

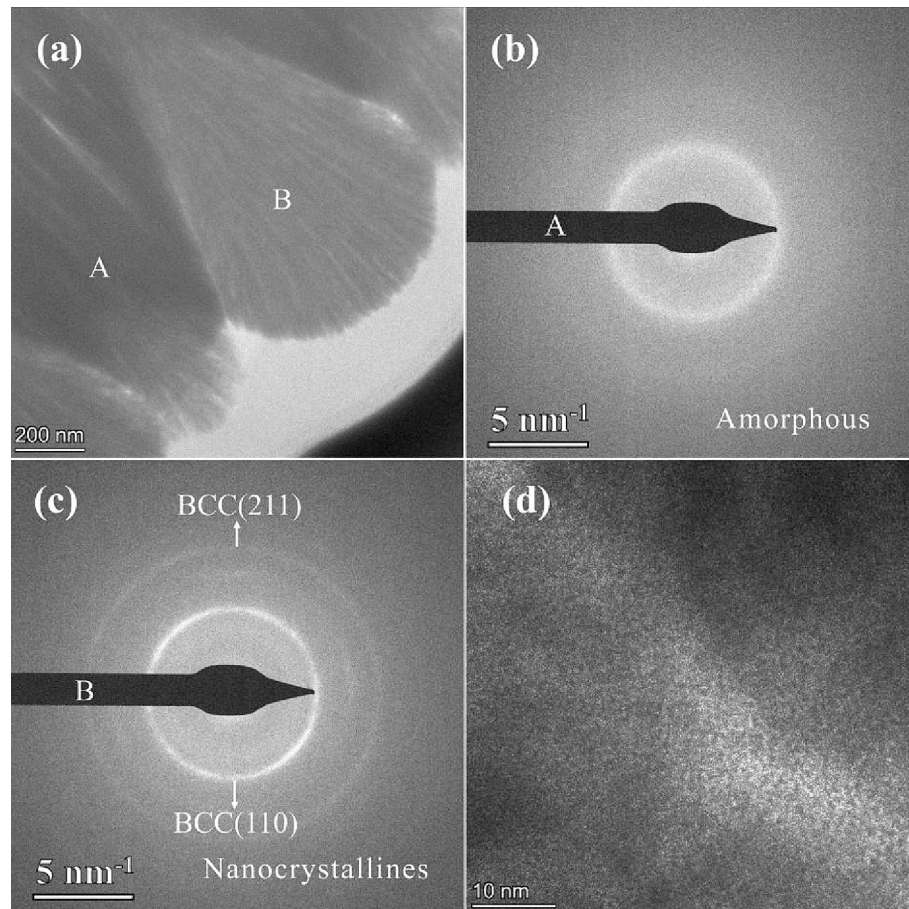


Fig. 6. TEM images of $(\text{MoTaWNb})_{1-x}\text{Y}_x$ RHEA film with 21.38 at.% Y additions: (a) bright-field TEM image, (b) (c) corresponding SAED, and (d) HRTEM image.

Fig. 5 displays the surface and cross-section SEM morphologies of Y-added $(\text{MoTaWNb})_{1-x}\text{Y}_x$ RHEA films at various powers. The morphology and structure of the films are significantly influenced by Y contents. The deposited films exhibit a structural change from fibrous-shaped to V-shaped columnar, and then to fibrous-shaped columnar of their cross-sectional morphologies, which corresponds to an increase in Y contents. The cross-sectional SEM images of films exhibit a fibrous and dense microstructure for 0, 28.63 at.%, and 37.49 at.% Y-added RHEA films (Fig. 5a1, d1, e1). On the other hand, the film density is decreased when Y content is 11.41 at.%, and the film cross-section reveals a

densely packed columnar microstructure with a significant amount of defects and nano-voids inside (Fig. 5b1). For 21.38 at.% Y-added RHEA films, the deposited film exhibits the most unusual morphology, with the fine fibrous-shaped columnar microstructure growing from the substrate and changing at half the thickness of the film. There are finally several comparatively rough V-shaped columnar microstructures with floral shapes (Fig. 5c, c1) on the smooth surface as a result of some of the fibrous-shaped columnar microstructure growing and spreading irregularly in all directions. The V-shaped columnar microstructure is a common nodular growth feature on deposited films. Whereas at higher

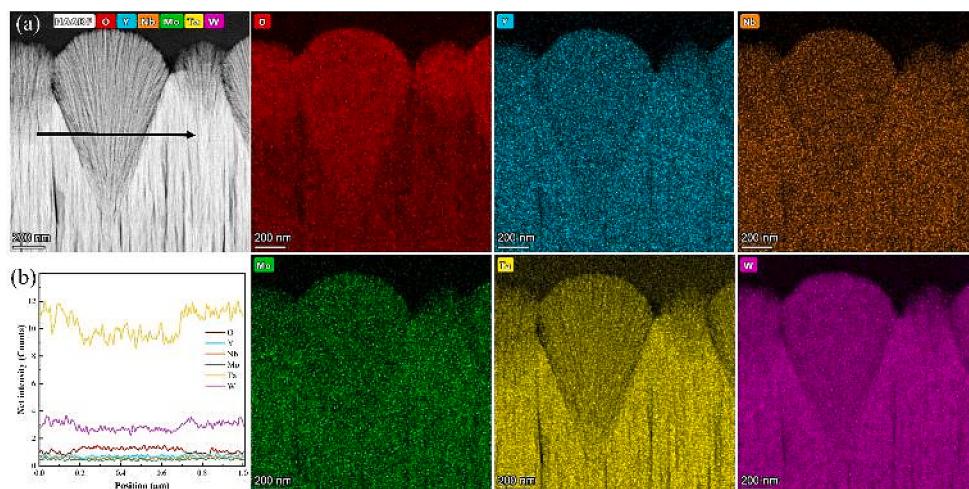


Fig. 7. HAADF-TEM micrograph, corresponding EDX maps and lines of $(\text{MoTaWNb})_{1-x}\text{Y}_x$ RHEA film with 21.38 at.% Y additions.

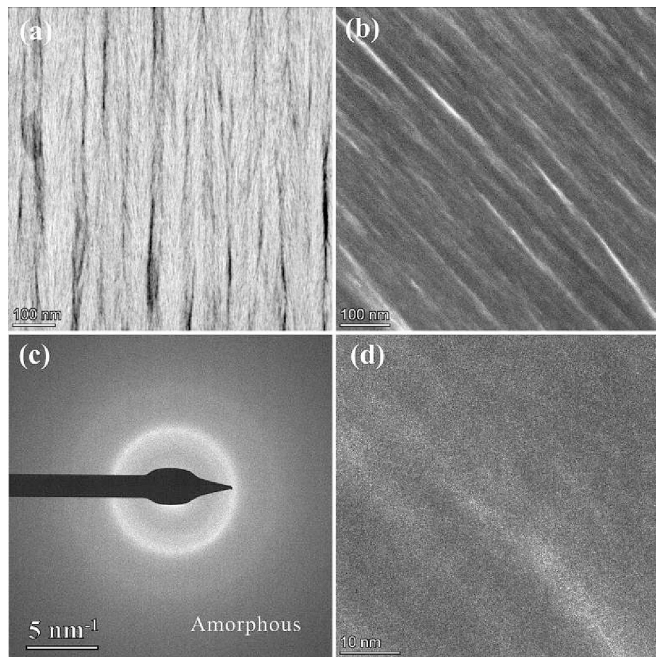


Fig. 8. TEM images of $(\text{MoTaWNb})_{1-x}\text{Y}_x$ films with 28.63 at.% Y additions: (a) STEM image, (b) bright-field TEM image, (c) corresponding SAED, and (d) HRTEM image.

Y-added to RHEA film, a small number of nanoscale cluster island structures appear on the surface of the film (Fig. 5d, 5d1), and it can be seen that the large islands indicate a hierarchical structure, which consists of smaller glassy particles. The temperature of the substrate, the rate of deposition, the angle of incidence, the vacuum environment, and the material itself all affect the microstructure of the films. When the mobility of the deposited atoms is restricted, the film is seen to display an array of parallel columns with a higher density [29–31]. When $T/T_m \leq 0.3\text{--}0.5$ (where T is the film's temperature and T_m is the material's melting temperature), the film-deposited atoms have low atomic

mobility, and the surface atoms move only 1–3 atomic positions and form an amorphous structure [32]. By limiting the interfacial and surface energies, this morphological shift of nanoscale cluster island formations is thought to be energetically advantageous, further lowering the total energy of the system [33,34]. Furthermore, a continuous and subsequent increase of micro-cracks is also observed with 37.49 at.% Y-added RHEA film. This could be the result of the thermal mismatch between the substrate and the coating or due to the presence of residual stress generated during the deposition, leading to the generation of micro-cracks that propagate across the deposited surface [35,36].

Through TEM investigations, the growth pattern of the V-shaped columnar microstructure on thin film is investigated. The bright-field TEM micrographs, selected area electron diffraction patterns (SAED), and high-resolution TEM (HRTEM) image of the as-deposited 21.38 at.% Y-added RHEA film are revealed in Fig. 6. It is evident from Fig. 6a that the film mostly consists of the fibrous-shaped columnar microstructure at the bottom film and the V-shaped columnar microstructure with an angle of about 50° in the surface, showing obvious interfaces between distinct microstructures. The two phases at positions A and B are demonstrated in the SAED results of Fig. 6b and c, respectively. The wider diffraction rings (Fig. 6b) and the atoms in the HRTEM image (Fig. 6d) show a disordered arrangement, indicating that the fibrous-shaped microstructure is poorly crystallized with an amorphous phase. On the other hand, the vivid diffraction rings of the V-shaped columnar microstructure suggest that this microstructure partially crystallizes, resulting in a BCC solid solution with a crystal structure with a textured orientation of (110). Fig. 7 displays the HAADF-STEM micrographs, corresponding EDX mappings, and line spectra of the 21.38 at.% Y-added RHEA film. This demonstrates different element distributions between the fibrous-shaped columnar microstructure and V-shaped columnar microstructures, showing lower Ta and W elements and higher O elements as slight segregation at the region of the V-shaped columnar microstructures. Furthermore, the amorphous phase is in a thermodynamically sub-stable state, which can be converted into a more stable crystalline state. Research has indicated that the slight segregation occurrence promotes crystallization with the variation in Gibbs free energy between the amorphous and crystalline states. Additionally, intrinsic tension stress induced by two phases within the film plays a

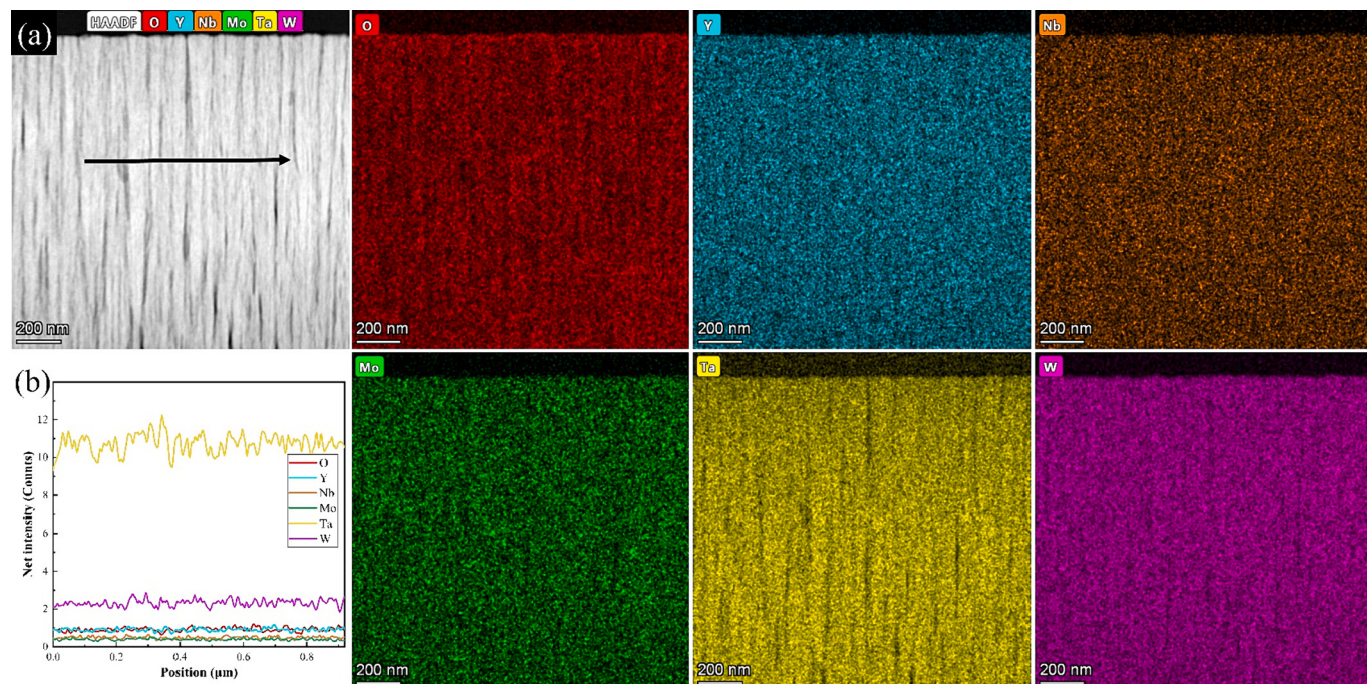


Fig. 9. HAADF TEM micrograph, corresponding EDX maps and line of $(\text{MoTaWNb})_{1-x}\text{Y}_x$ films with 28.63 at.% Y additions.

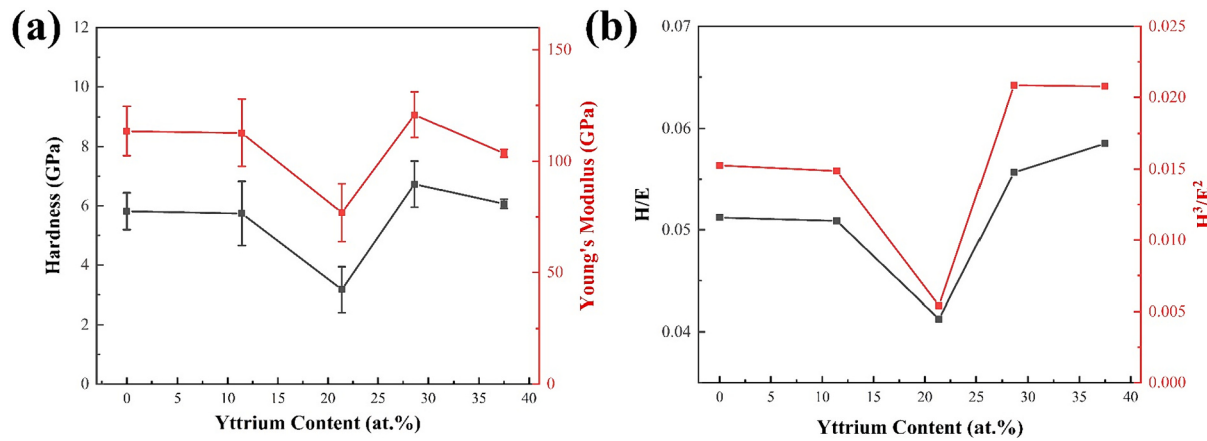


Fig. 10. Measurement results of nano-indentation of $(\text{MoTaWNb})_{1-x}\text{Y}_x$ RHEA films as function of Y content: (a) the hardness and Young's modulus, (b) the values of H/E and H^3/E^2 .

significant role in both the growth and crystallization of the microstructure [37,38]. Thus, it may be concluded that the formation of the V-shaped columnar microstructures is caused by partial crystallization of the amorphous microstructure due to slight segregation and internal stress changes.

TEM investigations were conducted on 28.63 at.% Y deposited film to obtain a detailed microstructure. Images from scanning transmission electron microscopy (STEM), bright field TEM, corresponding SAED, and HRTEM of the films are shown in Fig. 8. As observed in Fig. 8a and b, the film has a tightly condensed, fibrous-shaped columnar microstructure coupled with many dark stripes and nanoscale pores along the development direction. The diffraction ring encircled by diffusion halo rings in Fig. 8c and the atoms arranged completely at random in Fig. 8d exhibit characteristic amorphous qualities, suggesting that the deposited 28.63 at.% Y-added RHEA film has an entirely amorphous structure consistent with the XRD results. Fig. 9 shows the HAADF-TEM micrographs of the deposited film and the related EDX maps and lines to further detect the dark streaks at the interfaces between the fiber columnar microstructure. Except for dark streaks, all elements are evenly distributed. Other research has shown that dark streaks are formed due to the influence of the film's tensile internal stresses and that the deposited atoms have low energy and diffusion capacity on the substrate surface at low sputtering power. Moreover, the atoms that are deposited have sufficient energy to migrate at high sputtering power, meaning that the denser the microstructure [21,37].

3.4. Nano-mechanical properties of films

The mechanical properties of $(\text{MoTaWNb})_{1-x}\text{Y}_x$ films are

characterized by nano-indentation measurements as shown in Fig. 10, where H represents nano-hardness and E stands for Young's modulus, respectively. When the Y addition is changed from 0 at.% to 21.38 at.%, the mechanical characteristics of the films exhibit a slow to abrupt decline trend, as seen in Fig. 10a. The film with 21.38 at.% Y is notable for having the lowest nano-hardness, which is mostly because of the coarser V-shaped columnar microstructure that predominates in the film and degrades its mechanical properties. With the Y content of 28.63 at.%, H and E of RHEA films continuously increase to the maximum values of 6.74 GPa and 120.96 GPa, respectively. The highest hardness can be attributed to solid solution strengthening as the result of severe lattice distortion, which is brought on by the addition of large-sized Y atoms. The denser fibrous-shaped columnar microstructure also considerably enhances the hardness of the films. Due to the generation of micro-cracks, H and E of 37.49 at.% Y-added RHEA films are declined. In the meantime, two crucial mechanical characteristics of $(\text{MoTaWNb})_{1-x}\text{Y}_x$ films are the ratio of H/E and H^3/E^2 , which represent the material's resistance to plastic deformation and elastic strain fracture, respectively [22,33]. The findings are displayed in Fig. 10b, where it is evident that the evolution of the mechanical properties and the changes in H/E and H^3/E^2 are essentially the same. This suggests that a reasonable concentration of Y ranging from 28.63 at.% to 37.49 at.% can enhance the resistance to plastic deformation of films. Typical load-displacement ($P - h$) curves for deposited films with an indentation depth of about 500 nm are shown in Fig. 11. The $P - h$ curve illustrates the film's plastic deformation process, and jitter during the loading phase is directly related to inhomogeneous plastic deformation of the amorphous phase, as can be shown in Fig. 11(b). Plastic deformation in amorphous alloys is intrinsically unstable, and it experiences highly

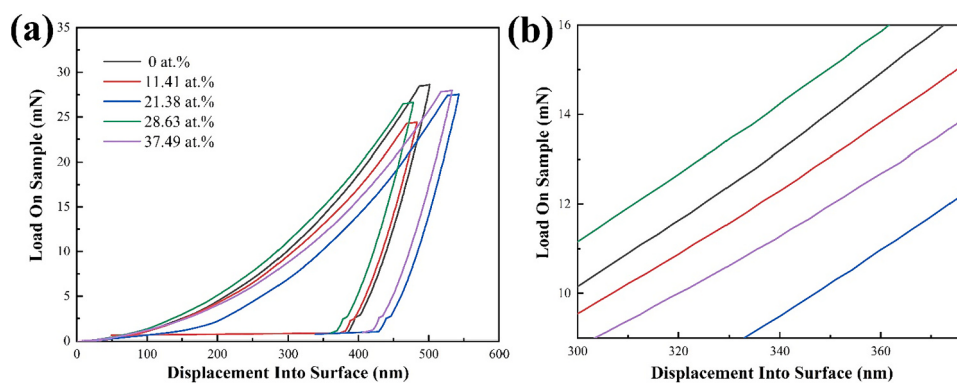


Fig. 11. Nano-mechanical properties of $(\text{MoTaWNb})_{1-x}\text{Y}_x$ RHEA films: (a) the representative load-displacement curves, (b) local magnification of load-displacement curves in range of 300–395 nm for displacement into surface.

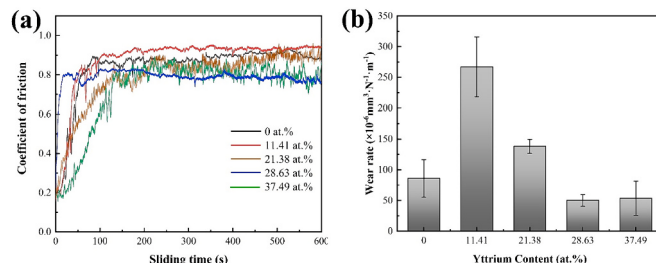


Fig. 12. Friction and wear results of the $(\text{MoTaWNb})_{1-x}\text{Y}_x$ films: (a) The coefficient of friction, (b) wear rate.

localized strain bursts in the shear zone and displays irregular flow characteristics [39].

3.5. Friction and wear behaviors of films

The friction coefficient curves and wear rates of the deposited $(\text{MoTaWNb})_{1-x}\text{Y}_x$ films are shown in Fig. 12, which shows that the Y-element content and morphology have a large influence on the friction and wear properties of the films. The films experience two wear stages: running-in wear and steady-state wear, as shown in Fig. 12a. The surface of the films is relatively rough, the actual contact area is small, and the surface is rapidly crushed by extrusion and deformation under the action of larger stress during the running-in wear stage when the grinding ball and the film surface are just in contact. This effectively suppresses the sharp fluctuation of contact stress and causes the friction coefficient curve to grow steadily during the running-in wear period [4]. After entering steady-state wear, the wear behavior of the deposited films is slow and stable, with steady-state friction coefficients in the range of 0.75–0.95. With the smallest floating friction coefficient and the shortest running-in wear period, the 28.63 at.% Y-added film exhibits good friction stability. As the Y element increased, the wear rate is 86.2×10^{-6} , 267.1×10^{-6} , 138.2×10^{-6} , 50.4×10^{-6} , and 53.7×10^{-6} $\text{mm}^3 \cdot \text{N}^{-1} \cdot \text{m}^{-1}$ for 0, 11.41, 21.38, 28.63, and 37.49 at.% Y-added films, respectively. The wear rate of the films increases first and then decreases, which is closely related to the resistance to plastic deformation and elastic strain fracture of $(\text{MoTaWNb})_{1-x}\text{Y}_x$ RHEA films. The

coarsened columnar with micro-cracks in the microstructure for the 11.41 at.% Y-added RHEA film shows the highest wear rate. The V-shaped columnar microstructure in the 21.38 at.% Y-added RHEA film exhibits significantly lower wear resistance due to inferior plastic deformation and elastic strain fracture of this film. On the contrary, the superior wear resistance is displayed in the Y-added RHEA films with the fine fibrous-shaped columnar microstructure with higher plastic deformation and elastic strain fracture.

To further determine the wear mechanism of the films, the worn surface morphology of represented $(\text{MoTaWNb})_{1-x}\text{Y}_x$ RHEA films with 21.38 at.% and 28.63 at.% Y additions are observed using SEM, as illustrated in Fig. 13. The worn RHEA film exhibits a rough wear surface, which is characterized by many grooves and convex adhesion layers. There are elongated grooves that slide out of the film's wear surface due to hard particles or protrusions, which suggests that abrasive wear has occurred. Table 3 shows the chemical composition of various wear areas (shown in Fig. 13). It is evident that the wear surface of RHEA films has undergone oxidation. The friction heat and contact stress will encourage the sintering and adhesion of the debris particles, causing some oxide layers to adhere to the wear surface and form an adhesion layer. Most of the oxide layer on the film is severely cracked and is very easy to peel off from the wear surface, seriously reducing its wear resistance. At the same time, trace Si elements were found in the adhesion layer, indicating that there was slight adhesive wear between the film and the friction pair. Part of the V-shaped columnar microstructures in the Y-added RHEA films are preserved and cause slight plastic deformation. Most of the V-shaped columnar fractures quickly in response to contact stress, generating wear debris up until it is flush with the wear surface (Fig. 13a1). Bhowmick et al. [40] revealed that the deformation

Table 3
Chemical composition of various worn regions in Fig. 13.

Region	Chemical composition (at.%)						
	Mo	Ta	W	Nb	Y	O	
A1	9.57	10.28	13.34	9.68	11.45	45.68	–
A2	5.91	6.28	8.28	5.99	7.14	64.29	2.11
B1	9.70	10.40	13.53	9.55	16.29	40.53	–
B2	4.86	5.50	7.28	4.99	8.53	65.73	3.11

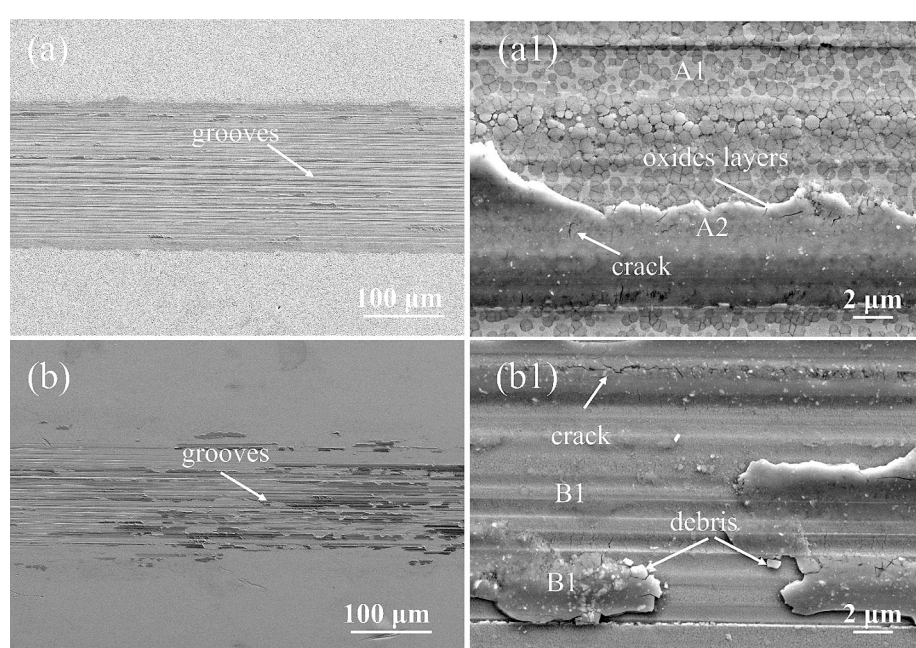


Fig. 13. Worn surface morphology of represented $(\text{MoTaWNb})_{1-x}\text{Y}_x$ film: (a) (a1) 21.38 at.% Y, (b) (b1) 28.63 at.% Y.

mechanism of the columnar structure film is mainly inter-column sliding. This deformation mechanism can distribute part of the applied load to the matrix of the peripheral and central slip zones of the column, which effectively improves the wear resistance of the films. In addition, under the action of cyclic shear stress, the nanoscale pores in the films will concentrate stress, providing conditions for the propagation of cracks, which will eventually lead to the fracture of the structure and delamination on the surface of the Y-added RHEA films. The above evidence shows that the wear mechanism of the Y-added RHEA films is mainly abrasive, oxidation, and delamination wear.

4. Conclusions

This work reports the effective preparation of $(\text{MoTaWNb})_{1-x}Y_x$ RHEA films by MS and a detailed investigation of the influence of Y additions on their microstructure and mechanical properties. The main conclusions are summarized as follows:

- (1) The $(\text{MoTaWNb})_{1-x}Y_x$ RHEA films exhibit a mixed microstructure of BCC and amorphous phases. With the increase in Y content, the crystallinity of the deposited films decreases, and the film has a typical amorphous structure when the Y addition is >28.63 at.%
- (2) The growth mechanism of the $(\text{MoTaWNb})_{1-x}Y_x$ RHEA films is affected by Y additions with varying internal stress and atomic diffusion. The V-shaped columnar microstructure of the 21.38 at. % Y-added RHEA film increases the surface roughness and reduces the mechanical properties. However, when Y addition is 28.63 at.%, the film with denser fibrous-shaped columnar microstructure exhibits a maximum nano-hardness of 6.74 GPa.
- (3) The friction coefficients of the deposited films stabilize around values of 0.75–0.95. The evolution of tribological behavior is consistent with the evolutions in microstructure and mechanical properties. The RHEA film with 28.63 at.% Y additions exhibits higher values of H/E and H^3/E^2 , showing excellent wear resistance with the lowest wear rate is $50.4 \times 10^{-6} \text{ mm}^3 \cdot \text{N}^{-1} \cdot \text{m}^{-1}$. The wear mechanisms can be attributed to a combination of abrasion, delamination, and oxidation wear.

CRediT authorship contribution statement

Cong Fang: Conceptualization. **Chao Zhang:** Writing – review & editing. **Shuaishuai Zhu:** Methodology. **Baosen Zhang:** Resources. **Yuxing Fan:** Software.

Declaration of competing interest

The authors declare that they have no known competing financial interests or personal relationships that could have appeared to influence the work reported in this paper.

Data availability

Data will be made available on request.

Acknowledgment

This work was supported by the National Natural Science Foundation of China (No.52275194) and the Postgraduate Research & Practice Innovation Program of Jiangsu Province (SJCX23_1163).

References

- [1] Y. Chen, Z.W. Dai, Z.J. Jian, High entropy metallic glasses: glass formation, crystallization and properties, *J. Alloys Compd.* 866 (2021) 158852, <https://doi.org/10.1016/j.jallcom.2021.158852>.
- [2] A.L. Greer, Confusion by design, *Nature* 366 (1993) 303–304, <https://doi.org/10.1038/366303a0>.
- [3] K. Zhao, X.X. Xia, H.Y. Bai, D.Q. Zhao, W.H. Wang, Room temperature homogeneous flow in a bulk metallic glass with low glass transition temperature, *Appl. Phys. Lett.* 98 (2011) 141913, <https://doi.org/10.1063/1.3575562>.
- [4] S.S. Zhu, Y.P. Wu, S. Hong, J.B. Cheng, Z. Wei B.S. Zhang, Microstructure, mechanical properties and tribological behaviors of $(\text{Co}_{0.33}\text{Ni}_{0.33}\text{Cr}_{0.23}\text{Mo}_{0.18})_{80-x}\text{Nb}_x(\text{B}_{0.3}\text{Si}_{0.7})_{20}$ high entropy amorphous alloy coatings, *J. Alloys Compd.* 942 (2023) 169055. doi:<https://doi.org/10.1016/j.jallcom.2023.169055>.
- [5] Y.Q. Xu, Y.H. Li, Z.W. Zhu, W. Zhang, Formation and properties of $\text{Fe}_{25}\text{Co}_{25}\text{Ni}_{25}(\text{P}, \text{C}, \text{B}, \text{Si})_{25}$ high-entropy bulk metallic glasses, *J. Non-Cryst. Solids* 487 (2018) 60–64, <https://doi.org/10.1016/j.jnoncrysol.2018.02.021>.
- [6] F.Y. Shu, B.L. Zhang, T. Liu, S.H. Sui, Y.X. Liu, P. He, B. Liu, B.S. Xu, Effects of laser power on microstructure and properties of laser cladded CoCrFeNiSi high-entropy alloy amorphous coatings, *Surf. Coat. Technol.* 358 (2019) 667–675, <https://doi.org/10.1016/j.surfcoat.2018.10.086>.
- [7] W. Li, P. Liu, P.K. Liaw, Microstructures and properties of high-entropy alloy films and coatings: a review, *Mater. Res. Lett.* 6 (2018) 199–229, <https://doi.org/10.1080/21663831.2018.1434248>.
- [8] Y.Y. Zhang, Z.B. Zhang, Z.X. Wang, W. Yao, X.B. Liang, Structure and properties of high-entropy amorphous thin films: a review, *Jom* 74 (2022) 794–807, <https://doi.org/10.1007/s11837-021-05107-w>.
- [9] P.P. Cui, W.L. Li, P. Liu, K. Zhang, F.C. Ma, X.H. Chen, R. Feng, P.K. Liaw, Effects of nitrogen content on microstructures and mechanical properties of (AlCrTiZrHfN) high-entropy alloy nitride films, *J. Alloys Compd.* 834 (2020) 155063, <https://doi.org/10.1016/j.jallcom.2020.155063>.
- [10] J.J. Wang, S.F. Kuang, X. Yu, L.Q. Wang, W.J. Huang, Tribomechanical properties of CrNbTiMoZr high-entropy alloy film synthesized by direct current magnetron sputtering, *Surf. Coat. Technol.* 403 (2020) 126374, <https://doi.org/10.1016/j.surfcoat.2020.126374>.
- [11] F. Cemin, M.J.M. Jimenez, L.M. Leidens, C.A. Figueroa, F. Alvarez, A thermodynamic study on phase formation and thermal stability of AlSiTaTiZr high-entropy alloy thin films, *J. Alloys Compd.* 838 (2020) 155580, <https://doi.org/10.1016/j.jallcom.2020.155580>.
- [12] C.Y. Cheng, J.W. Yeh, High-entropy BNbTaTiZr thin film with excellent thermal stability of amorphous structure and its electrical properties, *Mater. Lett.* 185 (2016) 456–459, <https://doi.org/10.1016/j.mattlet.2016.09.050>.
- [13] O.N. Senkov, G.B. Wilks, D.B. Miracle, C.P. Chuang, P.K. Liaw, Refractory high-entropy alloys, *Intermetallics* 18 (2010) 1758–1765, <https://doi.org/10.1016/j.intermet.2010.05.014>.
- [14] O.N. Senkov, G.B. Wilks, J.M. Scott, D.B. Miracle, Mechanical properties of $\text{Nb}_{25}\text{Mo}_{25}\text{Ta}_{25}\text{W}_{25}$ and $\text{V}_{20}\text{Nb}_{20}\text{Mo}_{20}\text{Ta}_{20}\text{W}_{20}$ refractory high entropy alloys, *Intermetallics* 19 (2011) 698–706, <https://doi.org/10.1016/j.intermet.2011.01.004>.
- [15] Y. Long, G.M. Zhang, J.X. Chen, A. Datye, S.H. Zhang, U.D. Schwarz, H.-T. Lin, F.L. Zhang, Effect of yttrium on phase composition and microstructure of FeCoNiAlCrB high entropy alloys, *Mater. Sci. Eng. A* 873 (2023) 145058. doi:<https://doi.org/10.1016/j.msea.2023.145058>.
- [16] D.H. Xu, G. Duan, W.L. Johnson, Unusual glass-forming ability of bulk amorphous alloys based on ordinary metal copper, *Phys. Rev. Lett.* 92 (2004) 245504, <https://doi.org/10.1103/PhysRevLett.92.245504>.
- [17] H.E. Xu, Y.L. Du, Y. Deng, Effects of Y addition on structural and mechanical properties of CuZrAl bulk metallic glass, *T. Nonferr. Metal. Soc.* 22 (2012) 842–846, [https://doi.org/10.1016/S1003-6326\(11\)61254-5](https://doi.org/10.1016/S1003-6326(11)61254-5).
- [18] S.D. Lu, X.X. Li, X.Y. Liang, J.H. He, W.T. Shao, K.H. Li, J. Chen, Effect of Y additions on the oxidation behavior of vacuum arc melted refractory high-entropy alloy $\text{AlMo}_{0.5}\text{NbTa}_{0.5}\text{TiZr}$ at elevated temperatures, *Vacuum* 201 (2022) 111069, <https://doi.org/10.1016/j.vacuum.2022.111069>.
- [19] G.R. Li, M. Liu, H.M. Wang, D. Zhang, F. Tang, C.W. Wang, Y.T. Zhao, G. Chen, X. Z. Kai, Effect of the rare earth element yttrium on the structure and properties of boron-containing high-entropy alloy, *Jom* 72 (2020) 2332–2339, <https://doi.org/10.1007/s11837-020-04059-x>.
- [20] J.J. Wang, Y.X. Liu, Y. Zhang, W.M. Cai, L.Q. Wang, L.W. Tang, Effect of substrate bias on the microstructure and mechanical and tribological properties of ZrNbTiMo refractory high entropy alloy film, *Surf. Coat. Technol.* 455 (2023) 129214, <https://doi.org/10.1016/j.surfcoat.2022.129214>.
- [21] Y.S. Kim, H.J. Park, S.C. Mun, E. Jumaev, S.H. Hong, G. Song, J.T. Kim, Y.K. Park, K.S. Kim, S.I. Jeong, Y.H. Kwon, K.B. Kim, Investigation of structure and mechanical properties of TiZrHfNiCuCo high entropy alloy thin films synthesized by magnetron sputtering, *J. Alloys Compd.* 797 (2019) 834–841, <https://doi.org/10.1016/j.jallcom.2019.05.043>.
- [22] E.E. Garah, L. Patout, A. Bouissil, A. Charai, F. Sanchette, The effect of yttrium addition on microstructure and mechanical properties of refractory TiTaZrHfW high-entropy films, *Coatings* 13 (2023) 1380, <https://doi.org/10.3390/coatings13081380>.
- [23] Z. Wang, C. Wang, Y.Lu. Zhao, J.J. Kai, C.T. Liu, C.H. Hsueh, Nanotwinned CoCrFeMnNi high entropy alloy films for flexible electronic device applications, *Vacuum* 189 (2021) 110249, <https://doi.org/10.1016/j.vacuum.2021.110249>.
- [24] D. Tsai, Z.C. Chang, B.H. Kuo, M.H. Shiao, S.Y. Chang, F.S. Shieh, Structural morphology and characterization of $(\text{AlCrMoTaTi})\text{N}$ coating deposited via magnetron sputtering, *Appl. Surf. Sci.* 282 (2013) 789–797, <https://doi.org/10.1016/j.apsusc.2013.06.057>.
- [25] Y. Zhang, Y.J. Zhou, J.P. Lin, G.L. Chen, P.K. Liaw, Solid-solution phase formation rules for multi-component alloys, *Adv. Eng. Mater.* 10 (2008) 534–538, <https://doi.org/10.1002/adem.200700240>.

- [26] S. Guo, C.T. Liu, Phase stability in high entropy alloys: formation of solid-solution phase or amorphous phase, *Prog. Nat. Sci.-Mater.* 21 (2011) 433–446, [https://doi.org/10.1016/S1002-0071\(12\)60080-X](https://doi.org/10.1016/S1002-0071(12)60080-X).
- [27] A. Takeuchi, A. Inoue, Classification of bulk metallic glasses by atomic size difference, heat of mixing and period of constituent elements and its application to characterization of the main alloying element, *Mater. Trans.* 46 (12) (2005) 2817–2829, <https://doi.org/10.2320/matertrans.46.2817>.
- [28] A.L. Greer, Metallic glasses, *Science* 267 (1995) 1947–1953, <https://doi.org/10.1126/science.267.5206.1947>.
- [29] R. Kowong, S. Denchitcharoen, T. Lertvanithphol, N. Triamnak, C. Chananonwathorn, K. Jaruwongrungsee, A. Klamchuen, P. Muthitamongkol, W. Phae-ngam, H. Nakajima, P. Songsiririthigul, M. Horprathum, Nanostructure optimization of Zr-W-Ti metallic glass thin films via multitarget co-sputtering with oblique angle deposition approach, *J. Alloys Compd.* 886 (2021) 161265, <https://doi.org/10.1016/j.jallcom.2021.161265>.
- [30] S.J. Zheng, Z.B. Cai, J.B. Pu, C. Zeng, S.Y. Chen, R. Chen, L.P. Wang, A feasible method for the fabrication of VAlTiCrSi amorphous high entropy alloy film with outstanding anti-corrosion property, *Appl. Surf. Sci.* 483 (2019) 870–874, <https://doi.org/10.1016/j.apsusc.2019.03.338>.
- [31] L. Liu, J.B. Zhu, C. Hou, J.C. Li, Q. Jiang, Dense and smooth amorphous films of multicomponent FeCoNiCuVZrAl high-entropy alloy deposited by direct current magnetron sputtering, *Mater. Design.* 46 (2013) 675–679, <https://doi.org/10.1016/j.matdes.2012.11.001>.
- [32] R.F. Messier, The nano-world of thin films, *J. Nanophotonics* 2 (2008) 021995, <https://doi.org/10.1117/1.3000671>.
- [33] A. Obeydavi, A. Shafyei, A. Rezaeian, P. Kameli, J.W. Lee, Microstructure, mechanical properties and corrosion performance of Fe₄₄Cr₁₅Mo₁₄Co₇C₁₀B₅S₅ thin film metallic glass deposited by DC magnetron sputtering, *J. Non-Cryst. Solids* 527 (2020) 119718, <https://doi.org/10.1016/j.jnoncrysol.2019.119718>.
- [34] N. Chen, R. Frank, N. Asao, D.V. Louzguine-Luzgin, P. Sharma, J.Q. Wang, G. Q. Xie, Y. Ishikawa, N. Hatakeyama, Y.C. Lin, M. Esashi, Y. Yamamoto, A. Inoue, Formation and properties of au-based nanograined metallic glasses, *Acta Mater.* 59 (2011) 6433–6440, <https://doi.org/10.1016/j.actamat.2011.07.007>.
- [35] X.C. Zhang, M. Watanabe, S. Kuroda, Effects of residual stress on the mechanical properties of plasma-sprayed thermal barrier coatings, *Eng. Fract. Mech.* 110 (2013) 314–327, <https://doi.org/10.1016/j.engfracmech.2013.08.016>.
- [36] A.S. Ebner, S. Jakob, H. Clemens, R. Pippan, V. Maier-Kiener, S. He, W. Ecker, D. Scheiber, V.I. Razumovskiy, Grain boundary segregation in Ni-base alloys: a combined atom probe tomography and first principles study, *Acta Mater.* 221 (2021) 117354, <https://doi.org/10.1016/j.actamat.2021.117354>.
- [37] D.C. Tsai, Z.C. Chang, B.H. Kuo, Y.S. Deng, E.C. Chen, F.S. Shieh, Effects of sputtering power on microstructure and mechanical properties of TiVCr films, *Vacuum* 125 (2016) 227–233, <https://doi.org/10.1016/j.vacuum.2015.11.015>.
- [38] P. Peter, D. Aljaz, G. Peter, C. Miha, P. Matjaž, Review of growth defects in thin films prepared by PVD techniques, *Coatings* 10 (2020) 447, <https://doi.org/10.3390/coatings10050447>.
- [39] C.A. Schuh, Nanoindentation studies of materials, *Mater. Today* 9 (2006) 32–40, [https://doi.org/10.1016/S1369-7021\(06\)71495-X](https://doi.org/10.1016/S1369-7021(06)71495-X).
- [40] S. Bhowmick, R. Bhide, M. Hoffman, V. Jayaram, S.K. Biswas, Fracture mode transitions during indentation of columnar TiN coatings on metal, *Philos. Mag.* 85 (2005) 2927–2945, <https://doi.org/10.1080/14786430500155213>.